

# An atoms-to-mesoscale approach to ice-vapor surface dynamics with a quasi-liquid interface

Steven Neshyba<sup>1</sup>, Tia Böttger<sup>1</sup>, Rohan Crossland<sup>1</sup>, Spencer Racca-Gwozdzik<sup>1</sup>, Ella Slattery<sup>1</sup>, Maximilian Bloom, Noah Zimmer<sup>1</sup>, Penny M. Rowe<sup>2</sup>, and Jacob Price<sup>1</sup>

<sup>1</sup>University of Puget Sound, Tacoma Washington USA

<sup>2</sup>North West Research Association, Redmond Washington, USA

## Abstract

*We explore the hypothesis that a key factor in determining the dynamics and morphology of faceted ice-vapor surfaces is the quasi-liquid layer that forms at this interface at temperatures above 240 K. We do so by modeling the ice surface as a system of reaction-diffusion equations in which the time scales of quasi-liquid freezing and melting, horizontal diffusion, and exchanges with the vapor phase are made explicit. Model parameterizations are informed by atomistic (molecular dynamics) simulations, mesoscale simulations of the vapor field around growing and ablating ice crystals, and quantitative ice surface morphologies derived from scanning electron microscope experiments. The outcome is a more unified, predictive, and experimentally grounded picture of the dynamics and morphology of faceted ice-vapor surfaces than has previously been presented.*

## Plain Language Summary

This is a mathematical exploration of the texture of ice surfaces on a microscopic scale. The main hypothesis is that this texture is governed by the behavior of a thin layer of water, intermediate between ice and liquid, that is known to form at the ice-air interface. We carry out this exploration by constructing a set of mathematical relationships that, when solved on a computer, reveal how parts of this quasi-liquid layer migrate to other regions of the ice surface, freeze, or evaporate into the air. The form and parameters of these equations are informed by insights and data from related work, including images of ice surfaces from scanning electron microscope experiments. We believe the insights obtained from this effort will be useful not only from a fundamental perspective, but also practically, especially in connection to the role of ice clouds in Earth's climate system.

## 1. Introduction

Why we care about ice crystal morphology ... the crystals that make up cirrus clouds modulate Earth's climate by reflecting or scattering sunlight before it reaches Earth's surface, but the extent to which they do that depends on the morphology of those crystals. Hexagonal prisms dominate, but there are lots of variations on that theme: long and thin hexagonal needles, short and wide plates, sometimes indented at the ends, or hollowed, or even dendritic forms, like snowflakes. Their surfaces can be smooth or rough on a scale that matters to light of comparable wavelength [Jarvinen et al, others].

Numerous models of ice surface morphology and dynamics during vapor depositional growth have been presented. Harrington and Pokrifka [2021] provide an excellent review. Of these, models rooted in atomistic structure and processes are appealing because of the evident connection between molecular structure on the one hand, and high-resolution microscopic observations (such as scanning electron microscopy) on the other; a familiar example is that crystals of water ice are understood to owe their hexagonal shape to the hexagonal structure of the unit cell of an ice lattice.

Of particular interest here is the Burton-Cabrera-Frank theory of crystal growth, also called classical nucleation theory, or CNT. CNT's atomistic view of the process of crystal growth goes along the following lines: when a gas-phase molecule (e.g., a water molecule) encounters a crystalline surface, it initially becomes attached to that surface as an "admolecule." Not yet part of the crystal's lattice, this admolecule diffuses across the surface until it meets one of two fates: either it fills an unoccupied position in the crystal lattice (often visualized as a step between ledges), or else it detaches from the surface and re-enters the gas phase.

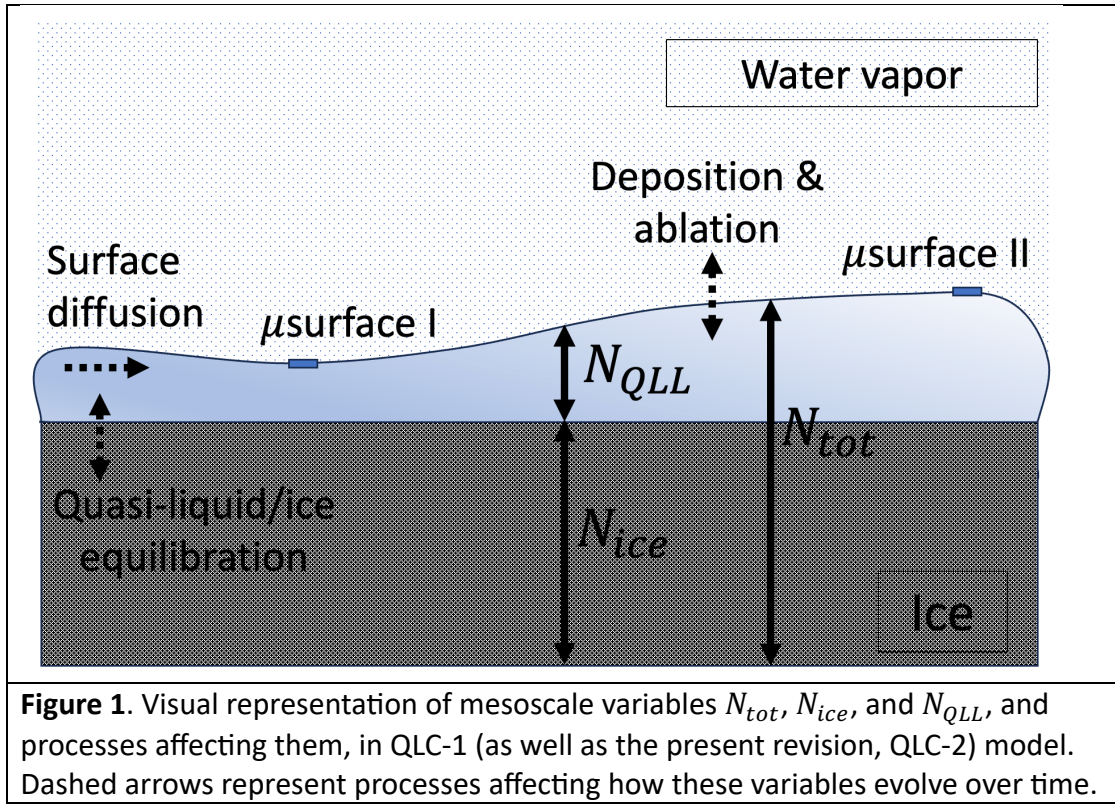
CNT has long framed how we think about ice crystal growth from the vapor phase, but it has significant shortcomings. One has to do with the resilience of faceting in growing crystals. When a faceted ice crystal is situated in a supersaturated vapor field, the corners of the crystal will experience persistently higher vapor pressures compared to facet centers. CNT predicts that this would result in faster growth at those corners, leading to indented crystal morphologies, and even dendritic forms (e.g., snowflakes). However, under some conditions, it's known that crystals resist that tendency, and instead maintain faceted – even when facets are large enough that excess admolecules at corners don't have enough time to diffuse to facet centers. There is an analogous issue when it comes to faceted crystals situated in a subsaturated vapor field, in which case the corners of the crystal will tend to experience persistently lower vapor pressure (again, compared to facet centers). CNT predicts that this would result in faster ablation at facet corners, eventually leading to a rounded crystal geometry. But in some conditions, crystals stubbornly maintain their faceted shape, despite lower vapor conditions at corners. Both cases just described can be summed up as a resilience of faceting that occurs under some conditions, despite persistent inhomogeneities in the overlying vapor field. Classical nucleation theory has no satisfactory explanation for this resilience.

To add to that criticism is the fealty (or lack of it) of CNT to what we know about the molecular structure of the ice-vapor interface. It is this: when the temperature of ice rises above 240 K, both experiment and theoretical studies have shown that there are no lattice gaps directly available to an admolecule on the ice surface, because the interface is entirely covered by a quasi-liquid layer (QLL). Molecular dynamics studies have shown that this QLL thermalizes nearly every water vapor molecule that impacts the surface, on a picosecond time scale. On the other hand, experimental work by Murata et al [2019] has shown that at the interface between the QLL and the underlying ice, there really are steps and ledges at that interface.

Bridging the gap between atomistic and mesoscale levels, therefore, would seem to require an atomistic model that begins with the existence of a QLL (above 240 K), preserving relevant

parts of CNT as much as possible. One such attempt was presented by some of the authors in 2016 (N2016), in the form of a dynamic quasi-liquid continuum model, referred to here as QLC-1. Because that model forms the foundation of the revision presented here (“QLC-2”), we summarize that framework next.

QLC-1 frames the problem of ice surface dynamics in terms of two mesoscale variables,  $N_{tot}$  and  $N_{QLL}$  (see Fig. 1), which represent the total number density of the ice surface and its quasi-liquid part, at any given point on the surface. Time evolution of these variables is governed by a pair of reaction-diffusion equations that represent the three processes indicated in Fig. 1, namely, (i) exchanges (deposition and ablation) of QLL molecules with the vapor phase, (ii) horizontal diffusion of QLL molecules across the ice surface, and (iii) interconversion of QLL molecules to/from the underlying ice.



The main insight afforded by QLC-1 is that it provides a mechanism by which faceted ice crystal growth can occur. At the heart of that mechanism is a process N2016 termed “diffusive slowdown,” which can be summarized as follows:

- 1) At the micrometer level, the QLL can be thought of as consisting of a continuum of microstates, ranging from a thin, less-volatile microstate labeled  $\mu_{\text{surface I}}$ , to a thick, more-volatile one labeled  $\mu_{\text{surface II}}$ . The difference in these volatilities is quantified in QLC-1 as a difference in equilibrium supersaturation,  $\sigma^o$ .

- 2) In a growing ice crystal, each time a new layer forms, a new pair of these microstates appears on the surface. Since new layers typically form at facet corners (where the water vapor concentration is highest), it is also the case that the horizontal distance between newly-formed ice layers is smaller at facet corners compared to facet centers. In this paper, we designate this distance as “ $\lambda$ ”; in Fig. 2(a) we see that  $\lambda_{corner} < \lambda_{center}$ .

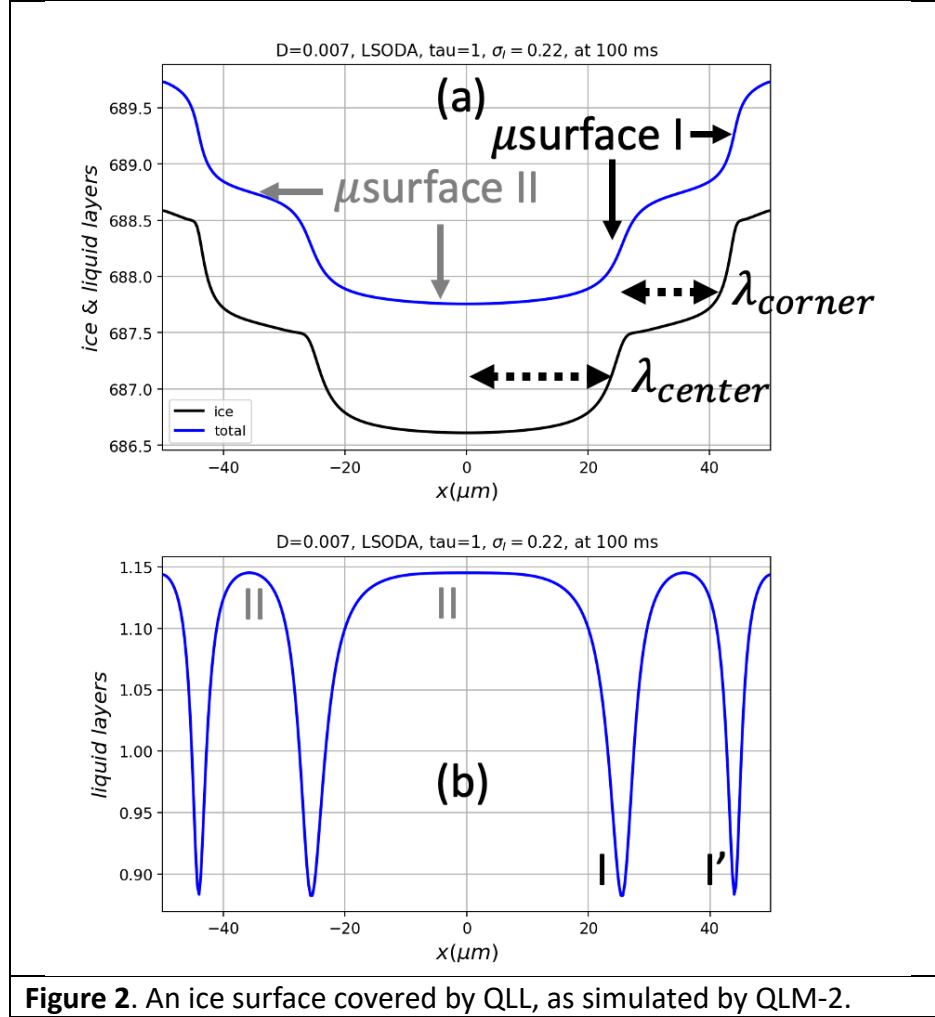


**Figure 2.** An ice surface covered by QLL, as simulated by QLM-2.

- 3) Horizontal diffusion moves quasi-liquid away from thicker,  $\mu_{surface II}$ -like regions of the surface, and toward thinner,  $\mu_{surface I}$ -like regions. However, because  $\mu_{surface I}$  accounts for a smaller fraction of the total surface area (as seen in Fig. 2(b)), diffusion has a greater proportional effect on it. As a consequence, diffusion leads to an increase in the average volatility of the surface, causing the surface as a whole to experience a net “diffusive slowdown” in its growth rate. (The reader is referred to N2016 for a quantitative version of this argument.)

A second process identified in N2016 is that diffusive slowdown is not homogeneous across a facet. Instead, in a growing ice crystal, more diffusive slowdown occurs at facet corners. The reason is as follows:

- 4) In regions where  $\lambda$  is small, QLL thickness gradients are large. In Fig. 2(b), for example, it is clear that the gradient in QLL thickness at  $l'$  is greater than at  $l$ . It follows that, in a growing ice crystal, more diffusive slowdown occurs at facet corners.

In summary, a flat facet exposed to supersaturated vapor will initially experience an enhancement in growth rate its corners, because of increased vapor concentration there. But that same enhancement leads to more diffusive slowdown at corners, as new layers of ice become more tightly spaced there. When these effects evolve into balance – which can (and does) occur as an emergent property of the equations of motion defining QLC-1 (and QLC-2, as we will show here), the result is equal growth rates across the entire facet. That steady state, in turn, is interpreted at the mesoscale (e.g., in a high-resolution optical or scanning electron microscopy) as faceted growth.

QLC-1 suffered from some structural deficiencies, however, of which the most important for our present purpose is that the time scale of process (iii) illustrated in Fig. 1, the interconversion of quasi-liquid and ice, was fixed relative to processes (i) and (ii). In real crystal facets, these time scales are expected to vary from facet to facet, or as a function of temperature and vapor pressure. These time scales should therefore be adjustable quantities within the theory.

Our goal in this communication is to evaluate strengths and weaknesses of a revised quasiliquid continuum model for ice crystal growth and ablation designed to address this deficiency. Section 2 presents such a model, referred to here as QLC-2. Section 3 (with details given in Appendix 1) summarizes scanning electron microscopy (SEM) image processing algorithms that can be used to construct quantitative ice surface morphologies. Section 4 (with details given in Appendix 2) summarizes results from independent gas-phase simulations, the Vapor Field code, that can be used to inform parameterizations of QLC-2 having to do with the vapor field in contact with growing ice crystals. Section 5 describes parameterization strategies used to run QLC-2. Section 6 presents simulations and SEM experiments in pursuit of five lines of investigation. Section 7 discusses implications of these results in other contexts, including cirrus ice crystal morphologies and ideas from nonlinear dynamics.

## 2. QLC-2: A revised quasi-liquid reaction-diffusion model

Like QLC-1, QLC-2 represents an ice surface as two mesoscale variables and three processes, as shown in Fig. 1. The governing equations are

$$\frac{dN_{tot}}{dt} = D\nabla^2 N_{QLL} + v_{kin}\sigma_m \quad (1a)$$

$$\frac{dN_{QLL}}{dt} = \frac{dN_{tot}}{dt} - (N_{QLL} - N_{QLL}^{eq}(N_{tot}))/\tau_{eq} \quad (1b)$$

Some notes about this model are as follows, with differences between it and QLC-1 noted where relevant:

- 1)  $D\nabla^2 N_{QLL}$  represents surface diffusion of the QLL; the underlying ice is considered immobile on time scales considered here.
- 2)  $\nu_{kin}$  is the rate at which vapor-phase water molecules collide with the quasi-liquid; it is assumed that these stick with 100% efficiency, and thermalize on a picosecond time scale.
- 3)  $N_{QLL}^{eq}(N_{tot})$  prescribes the thickness of quasi-liquid when it is in equilibrium with the underlying ice, according to

$$N_{QLL}^{eq}(N_{tot}) = \bar{N} - N^* \sin(2\pi N_{tot}) \quad (2)$$

This formulation ensures that the QLL thickness varies continuously from the thin microstate (“ $\mu$ surface I”) with thickness  $\bar{N} - N^*$ , to the thick microstate (“ $\mu$ surface II”) with thickness  $\bar{N} + N^*$ . (Connection to work by MacDowell’s group [Benet et al 2020, Eq. 8], that also shows a sinusoidal dependence.)

- 4) Because  $\mu$ surfaces I and II have different volatilities, the surface supersaturation at a given point on the surface (designated  $\sigma_m$  in Eq. 1a) is a function of both the microstate and the water vapor concentration above it. To compute  $\sigma_m$ , we define a variable  $m$  that quantifies the degree to which a given surface is similar to  $\mu$ surface I or II,

$$m = \frac{N_{QLL} - (\bar{N} - N^*)}{2N^*} \quad (3)$$

With this definition,  $\mu$ surface I will have  $m = 0$ , while  $\mu$ surface II will have  $m = 1$ . We then express the surface supersaturation as

$$\sigma_m(x) = \sigma_I(x) - m\sigma^o \quad (4)$$

where  $\sigma^o$  is a measure of the difference in the equilibrium vapor pressure of  $\mu$ surfaces I and II, and  $\sigma_I(x)$  is the supersaturation relative to  $\mu$ surface I. We will assume here that both  $\sigma^o$  (a scalar quantity) and  $\sigma_I(x)$  are fixed parameters of a given trajectory. Eq. 4 is at slight variance with, and simpler than, the corresponding expression in QLC-1.

- 5) Typically, a parabolic form is used for  $\sigma_I(x)$  appearing in Eq. 4,

$$\sigma_I(x) = \sigma_{I,corner} \times \left( c_r \left( \frac{x}{L} \right)^2 + (1 - c_r) \right) \quad (5)$$

Here,  $c_r$  is a “center reduction”, the fractional lowering of supersaturation at facet centers compared to facet corners. Negative values of  $c_r$  are also used in the simulations presented here, to represent the fractional enhancement of water vapor concentration at facet centers when a crystal is subjected to ablation conditions.

- 6)  $\tau_{eq}$  is a first-order relaxation constant describing the time scale at which quasi-liquid/ice equilibrium is achieved. That is, if we imagine a surface with quasi-liquid amount  $N_{QLL}^o$ , then equilibration after a time  $\Delta t$  occurs according to

$$N_{QLL}(t) = N_{QLL}^{eq}(N_{tot}) + \left( N_{QLL}^o - N_{QLL}^{eq}(N_{tot}) \right) e^{-\frac{\Delta t}{\tau_{eq}}} \quad (6)$$

If one takes the time derivative of Eq. 6, and assumes that  $\Delta t$  is small, the second term on the right-hand side of Eq. 1b results.

Equations 6 and 1b represent the primary departure of QLC-2 from QLC-1. With this revision, we are able to specify the rate of quasi-liquid/ice equilibration relative to processes (i) and (ii). Specifying a small value for  $\tau_{eq}$ , for example, would represent the idea that quasi-liquid/ice equilibration is fast compared to those processes, while large  $\tau_{eq}$  would mean the opposite. We do not have reliable observational values of  $\tau_{eq}$ , but we do have a guidepost: because the “diffusive slowdown” mechanism for stabilization of faceted ice growth described above requires that quasi-liquid/ice equilibration be slow compared to surface diffusion, we should not be surprised if we find that large  $\tau_{eq}$  leads to stable growth dynamics. We return to this topic below.

### 3. ESEM/GNBF retrievals

Environmental SEM of imaging of ice crystals has seen considerable development in recent years, including the ability to image actively growing and ablating crystals by manipulating the temperature and pressure inside an SEM chamber. In tandem with those developments are computer codes for generating quantitative surface morphologies using a Gauss-Newton in a Bayesian Framework (GNBF) algorithm. The combination – a process we will refer to here as “ESEM/GNBF retrieval” – provides opportunities for vetting model predictions of surface morphology against experiment at resolutions that are not quite commensurate with one another, but approaching that level. Details are given in Appendix 1.

### 4. Vapor field simulations

QLC-2 requires numerous parameterizations. Some of these were provided, in N2016, by molecular dynamics simulations, and some by experimental observations. Unexploited in N2016, however, was the use of gas-phase simulations to define properties of  $\sigma_I(x)$ , the vapor concentration overlying a given ice surface. These simulations show that the parabolic form for  $\sigma_I(x)$ , given in Eq. 5, is an accurate representation of the surface water vapor concentrations under constant far-field concentrations of water vapor; they also provide a means of parameterizing of  $c_r$  as a function of the size of the crystal ( $L$ ), as well as the ambient temperature and air pressure. As described below, other forms may also be imposed as a way of exploring effects of perturbations to the ice surface. Details about these gas-phase simulations are given in Appendix 2.

### 5. Parameterizations

For the purpose of exploring solutions to the QLC-2 equations of motion, it is necessary to define values of the parameters appearing in Eqs. 1-6. To do so, we employed two separate strategies.

### Strategy A – Standalone QLC-2

In Strategy A, model parameters are explicitly specified as inputs:

- $L$ , distance from facet center to corner.
- $D$ , surface diffusion coefficient
- $v_{kin}$ , Hertz-Knudsen deposition velocity
- $\tau_{eq}$ , ice-QLL equilibration time constant.
- $\sigma_{I,corner}$  and  $C_r$ , which describe a parabolic representation of  $\sigma_I(x)$ .

The chief advantage of Strategy A is its simplicity. A disadvantage, however, is that in real life, some of these values are actually related to one another. One prominent example is that  $D$  and  $v_{kin}$  should both increase with increasing temperature. Another is that as a crystal gets larger (bigger  $L$ ), the reduction in the overlying supersaturation at facet centers should get bigger, compared to facet corners. These interdependencies are conveniently ignored in Strategy A.

### Strategy B – Integrated QLC-2 + Vapor Field

In Strategy B, some model parameters are explicitly specified (as in Strategy A), but others are made functions of ambient conditions, or decided upon on the basis of consistency with what is going on in the vapor surrounding the crystal. To summarize, explicitly specified parameters are:

- $L$ , distance from facet center to corner.
- $T$  and  $P_{amb}$ , temperature and pressure surrounding the crystal.
- $\sigma_{I,\infty}$ , supersaturation of water vapor far from the crystal.
- $\tau_{eq}$ , the ice-QLL equilibration time constant.

while others are obtained as follows:

- The surface diffusion coefficient is obtained from the ambient temperature,

$$D = D^o \exp\left(-\frac{E_a}{R} \left(\frac{1}{T} - \frac{1}{T_o}\right)\right) \quad (7)$$

with  $E_a = 22.8 \frac{kJ}{mol}$  and  $D^o = 9.20 \times 10^{-4} \frac{\mu m^2}{\mu s}$ , based on a fit to diffusion data of Price et al.

- The Hertz-Knudsen deposition speed is also temperature-dependent,

$$v_{kin} = P_{vap}^{eq}(T) \times \left(\frac{M_{H_2O}}{2\pi RT}\right)^{1/2} \quad (8)$$



where  $P_{vap}^{eq}(T)$  is water's equilibrium vapor pressure, and  $M_{H_2O}$  is its molar mass.

- The diffusivity of water vapor through air (required by the Vapor Field code) is a function of ambient temperature *and* ambient pressure, described in Appendix 2.
- $g_{ice}$ , the growth rate of the ice surface, is supplied iteratively, as follows:
  1. A Vapor Field simulation takes growth rate of the ice surface ( $g_{ice}$ ) as an input, along with  $L$ ,  $T$ ,  $P_{amb}$ , and  $\sigma_{I,\infty}$ , and predicts  $\sigma_{I,corner}$  and  $c_r$ .
  2. A QLC-2 simulation takes  $\sigma_{I,corner}$  and  $c_r$  as inputs, along with  $L$ ,  $T$ ,  $P_{amb}$ , and  $\sigma_{I,\infty}$ , and predicts a new growth rate of the ice surface ( $g'_{ice}$ ).
  3. Steps 1 and 2 are repeated until  $g_{ice}$  and  $g'_{ice}$  agree within some tolerance level.\

The chief disadvantage of Strategy B is its relative complexity, and the fact that the iteration just described makes the computation slower. Its main advantage is that connections to physical conditions are more transparent and self-consistent.

Common to both strategies were the following fixed values:

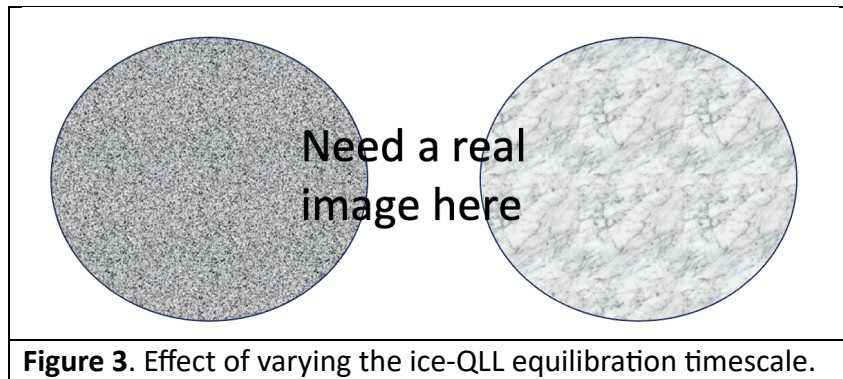
- $\bar{N}$  and  $N^*$ , representing the difference in equilibrium number density between  $\mu$ surfaces I and II (fixed at 1 and 0.143).
- $\sigma^o$ , the amount by which the equilibrium vapor supersaturation of  $\mu$ surface II exceeds that of  $\mu$ surface I (fixed at 0.2).
- $\Delta_N$ , the thickness of a single layer of ice (fixed at 0.3 nm).

## 6. Results

Here we describe the results of five lines of investigation we have pursued, each focusing on a particular topic or question. ESEM/GNBF and gas-phase modeling results are presented alongside, as relevant.

### I. Effect of variation in the time scale of modeled ice-quasiliquid equilibration

[still working on this, preliminary work says that bigger  $\tau$  stabilizes the formation of steady states, but otherwise has little effect on the shape of the steady-state profiles] ... See Fig. 3 ...



### II. Curvature of faceted surfaces undergoing growth and ablation

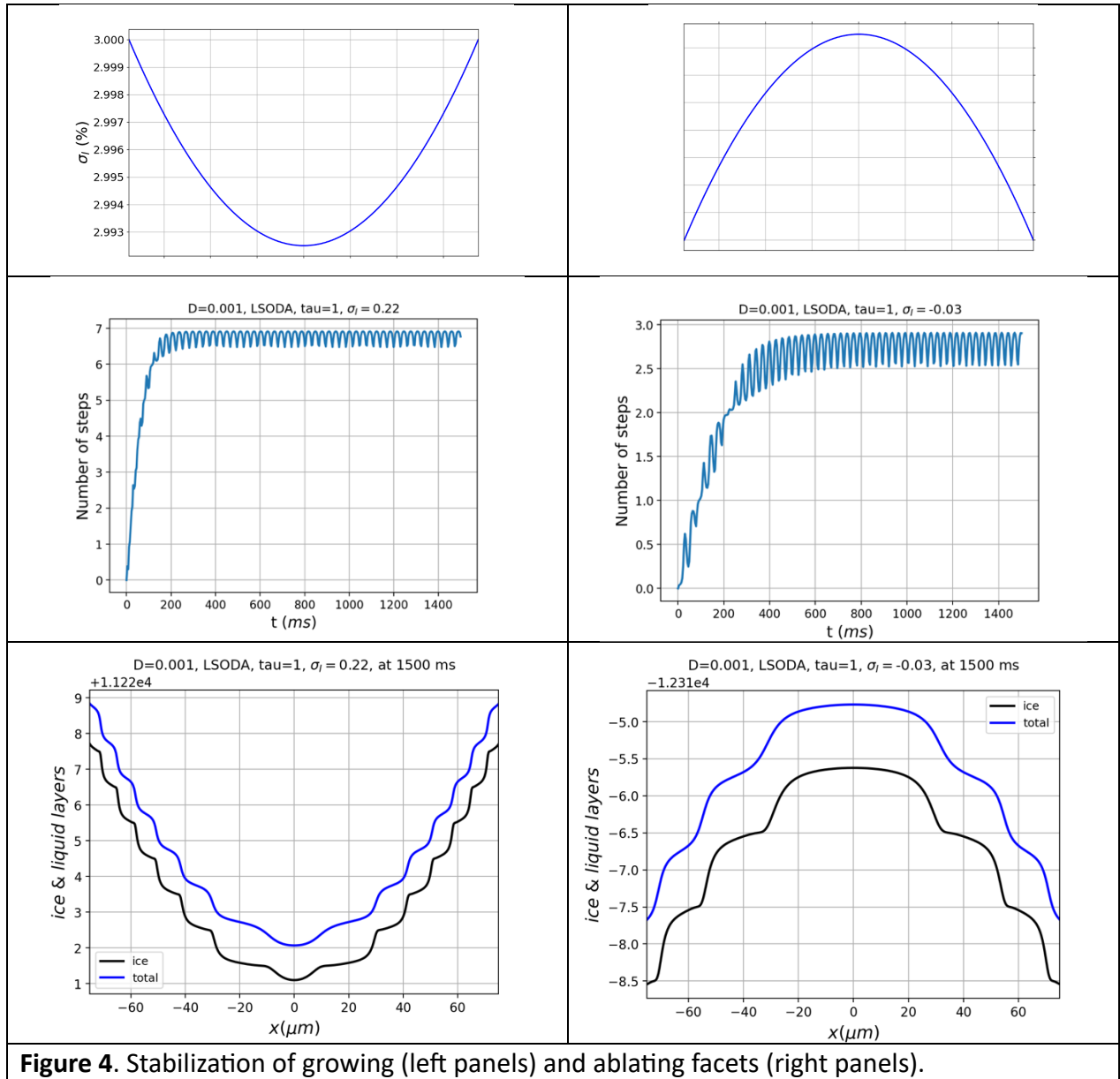
Figure 4 shows a modeled ice crystal surface under growing and ablating conditions. The growth scenario on the left of the figure resulted from supersaturated water vapor concentrations, distributed as shown in Fig. 4(a). Figures 4(b) and 4(c) show that these conditions lead to steady state, “V”-shaped profiles, in which the surface is dominated by primarily  $\mu_{\text{surface I}}$  – like microstates. This scenario exhibits more tightly bunched (smaller  $\lambda$ ) at facet boundaries, which in turn (as described above in the summary of diffusive slowdown) leads to a net increase in volatility of the surface as a whole, hence faceted growth.

The ablating scenario on the right of Fig. 4 resulted from subsaturated water vapor amounts, distributed as shown in Fig. 4(d). Figures 4(e) and 4(f) show that these conditions also lead to steady state, although in this case the profile is “ $\Lambda$ ” shaped (i.e., rounded), the surface is dominated by  $\mu_{\text{surface I}}$  – like microstates, and the layer bunching leads to *reduced* volatility of the surface near the corners, hence faceted ablation.

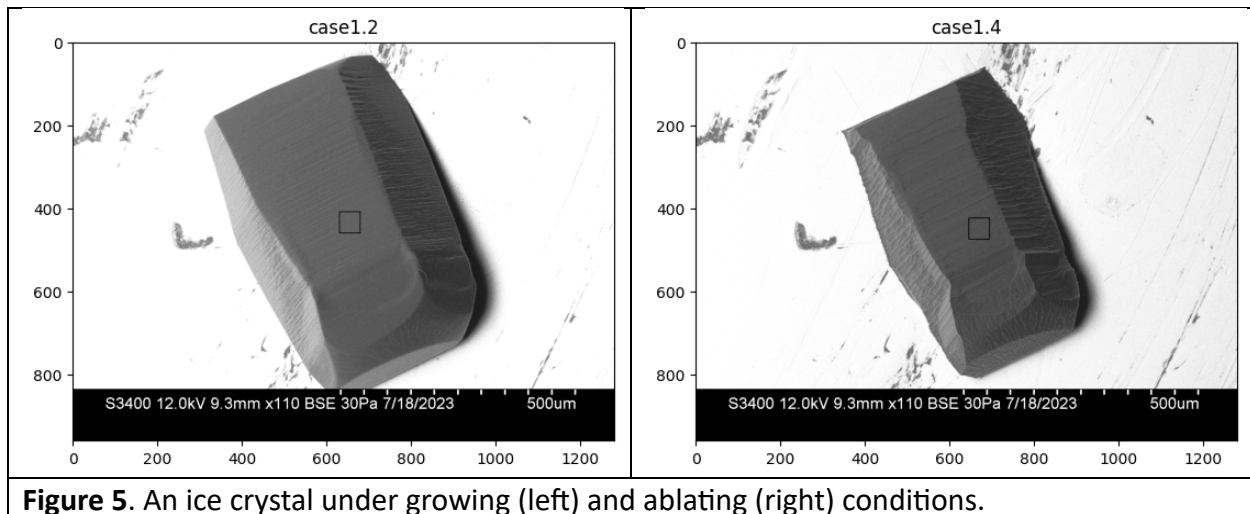
The model results shown in Fig. 4 also suggest the following general pattern: growing ice facets possesses convex curvature, whereas ablating ice facets possess concave curvature. A useful metric for describing the curvature of steady state profiles such as those appearing in Fig. 4 is the local slope of the surface. Here we quantify that slope as a mean horizontal distance between successive molecular layers, defined as

$$\bar{\lambda} = L/n_{\text{steps}} \tag{9}$$

For example, the growing facet profile on the left of Fig. 4 is characterized by  $\bar{\lambda} \approx 10 \mu\text{m}$ , whereas the ablating facet profile on the right is characterized by  $\bar{\lambda} \approx 25 \mu\text{m}$ .



It is well-known that real ice crystals exhibit faceted growth, but are they also capable of faceted ablation? Figure 5 displays ESEM images of an ice crystal observed under growing and ablating conditions. Since the ablating crystal retains its flat surface, we can conclude that faceted ablation has indeed occurred. The figure shows, moreover, that faceted ablation occurs even when the surface is rough (e.g., the prismatic facets in the figure). In fact, we observe faceted ablation quite frequently in ESEM images of ablating ice crystals.



Do real faceted ice crystals exhibit curvature like that indicated by the QLC-2 predictions of Fig. 4? Fig. 6(a) displays an ESEM image of a crystal and a GNBf construction of a portion of its basal facet. The crystal is known to be growing, since subsequent images taken of this crystal revealed expanding boundaries against the metal substrate to which the crystal is attached. The GNBf construction, displayed in Fig. 6(b), reveals a distinct convexity, on the order of 1000s of layers over the horizontal span analyzed ( $\sim 80 \mu\text{m}$ ) ... which corresponds to  $\bar{\lambda} \approx \dots$ .

Turning to ablation, Figs. 6(c-d) show an ESEM image of an ablating, faceted crystal, and its GNBf-constructed surface. *The GNBf reconstruction hopefully reveals concavity ....  $\bar{\lambda} \approx \dots$ .]*

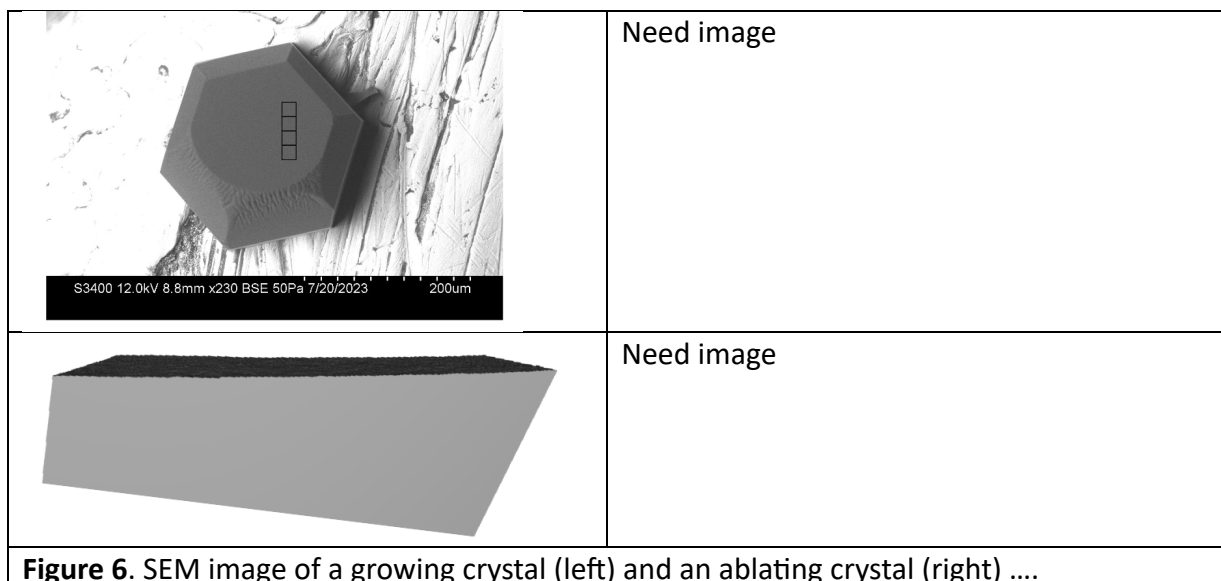


**Figure 6.** SEM image of a growing crystal (left) and an ablating crystal (right) ....

Thus, the pattern predicted by QLC-2 is borne out: growing ice facets do indeed exhibit facet convexity, while ablating ice facets exhibit facet concavity – although we hasten to point out that the  $\bar{\lambda}$  values are far smaller in the observations than in the model.

### III. Characteristic length scales of growing and ablating surfaces

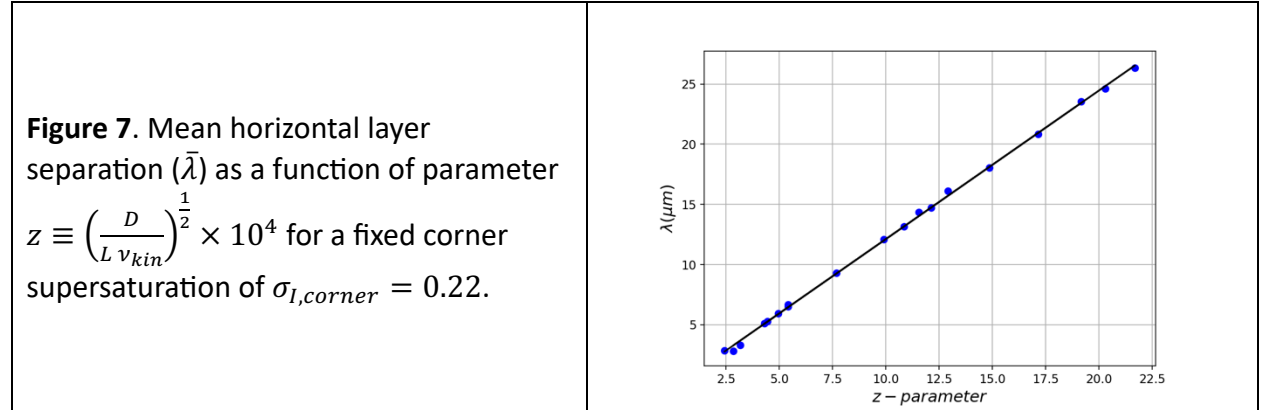
Here we investigate the possibility that growing and ablating ice crystals possess intrinsic length scales. Focusing first on observations, we note that a distinct growth/ablation asymmetry appears in the roughening evident in the ESEM images displayed in Fig. 5. ...

Figure 7 shows the dependence of the mean horizontal layer separation,  $\bar{\lambda}$  (introduced above), on the dimensionless parameter  $z$ , defined by

$$z \equiv \left( \frac{D}{L v_{kin}} \right)^{\frac{1}{2}} \times 10^4 \quad (10)$$

where (as described above)  $D$  is the surface diffusion coefficient,  $L$  is the edge length of the crystal, and  $v_{kin}$  is the kinetic deposition velocity. In constructing Fig. 7, components of  $z$  ranged in value as follows:

- $D = 1 \times 10^{-4}$  to  $8 \times 10^{-3} \frac{\mu m^2}{\mu s}$ ;
- $L = 8$  to  $160 \mu m$ ; and
- $v_{kin} = 12$  to  $250 \frac{\mu m}{s}$ .



It is clear from Fig. 7 that a good parameterization is

$$\bar{\lambda}_g = m_g z + b_g \quad (11)$$

where best-fit parameters are  $m_g = 1.235 \mu m$ ,  $b_g = -0.238 \mu m$ . Similar analysis of ablating wavelengths yields

$$\bar{\lambda}_a = m_a z + b_a \quad (12)$$

with  $m_a = \dots \mu m$  and  $b_a = \dots \mu m$ .

Figure 8 shows values of  $\bar{\lambda}$  for a range of corner supersaturations ( $\sigma_{I,corner}$ ), holding parameter  $z$  constant. We see that when conditions begin to become supersaturated,  $\bar{\lambda}_g$  starts off at about  $9 \mu m$  and declines monotonically, ultimately leading (we surmise) to hollowed or dendritic growth at high supersaturations. On the left-hand side are shown results when conditions are subsaturated. We see that under these conditions,  $\bar{\lambda}_a$  starts much higher than on the supersaturated side, at about  $30 \mu m$ , and declines monotonically with increasing subsaturation, ultimately leading (we surmise) to facet rounding.

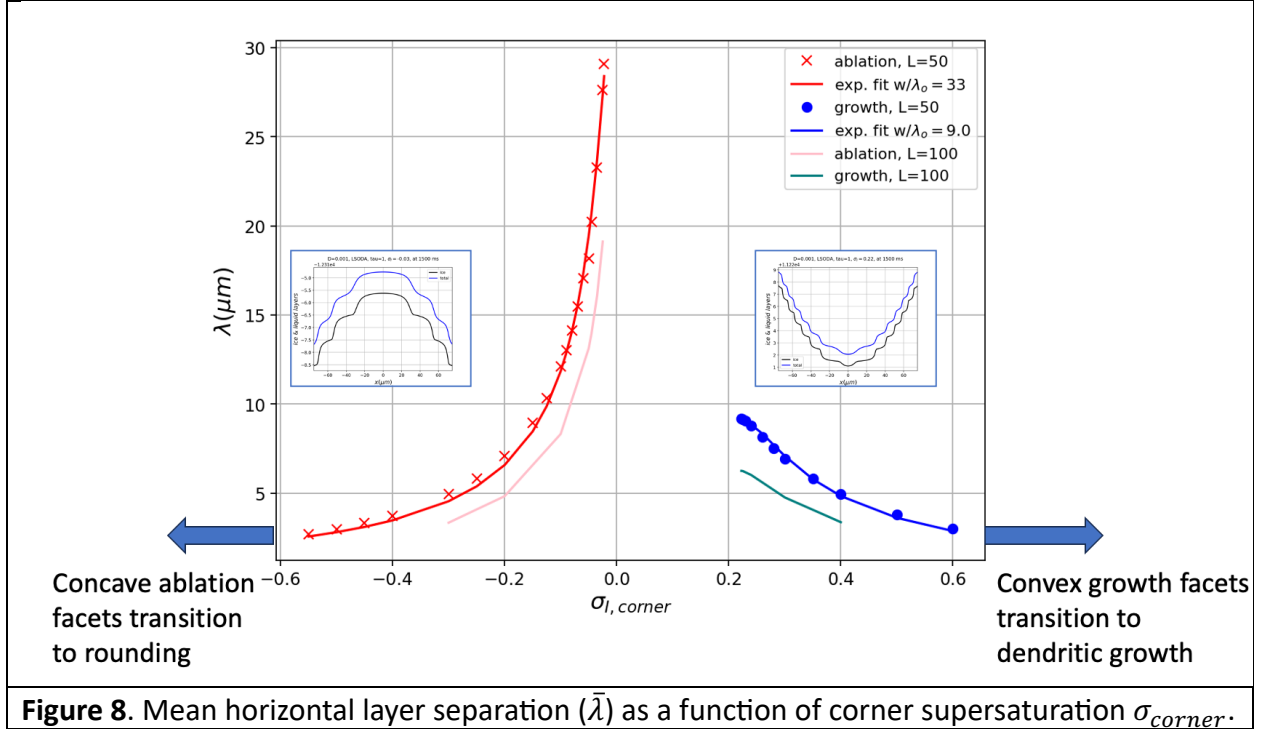


**Figure 8.** Mean horizontal layer separation ( $\bar{\lambda}$ ) as a function of corner supersaturation  $\sigma_{corner}$ .

We have carried out a best-fit analysis of the supersaturated-condition points on the right-hand side of Fig. 8, using an exponential, which when combined with the previous expressions (Eqs. 9 and 10) yield

Combining the above expressions, the functional forms are

$$\bar{\lambda}_g = \bar{\lambda}_{g,o} \times \left( 1 - \exp \left( - \frac{1}{(\sigma_{I,corner} - \sigma_o) x_{g,o}} \right) \right) \times \frac{m_g z + b_g}{m_g z_{ref} + b_g} \quad (13)$$

and

$$\bar{\lambda}_a = \bar{\lambda}_{a,o} \times \left( 1 - \exp \left( \frac{1}{(\sigma_{I,corner} - \sigma_o) x_{a,o}} \right) \right) \times \frac{m_a z + b_a}{m_a z_{ref} + b_a} \quad (14)$$

where

$$z_{ref} \equiv \left( \frac{D_{ref}}{L_{ref} v_{kin,ref}} \right)^{\frac{1}{2}} \times 10^4 \quad (15)$$

with  $D_{ref} = 1.0 \times 10^{-3} \frac{\mu m^2}{\mu s}$ ,  $L_{ref} = 50 \mu m$ , and  $v_{kin,ref} = 34 \frac{\mu m}{s}$ .

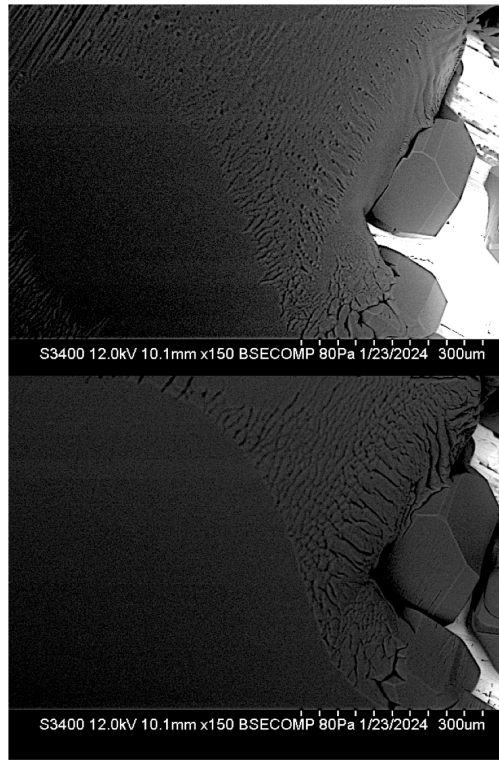
Figure 8 shows the results of applying this functional form to the numerical data, using best-fit parameters  $\bar{\lambda}_{g,o} = 9.65 \mu m$ ,  $x_{g,o} = 6.34$ ,  $\bar{\lambda}_{a,o} = 37.1 \mu m$ ,  $x_{a,o} = 23.7$ . The fit is pretty good ... And what it means is, we can predict steady-state properties over a very big range of physical variables (crystal length, surface diffusivity,  $v_{kin}$ , and imposed supersaturations).

Thus, both theory and experiment support the existence of characteristic length scales as a function of super/subsaturation. We hasten to add that the scale of these phenomena is vastly different ....

#### *IV. Resilience of steady states*

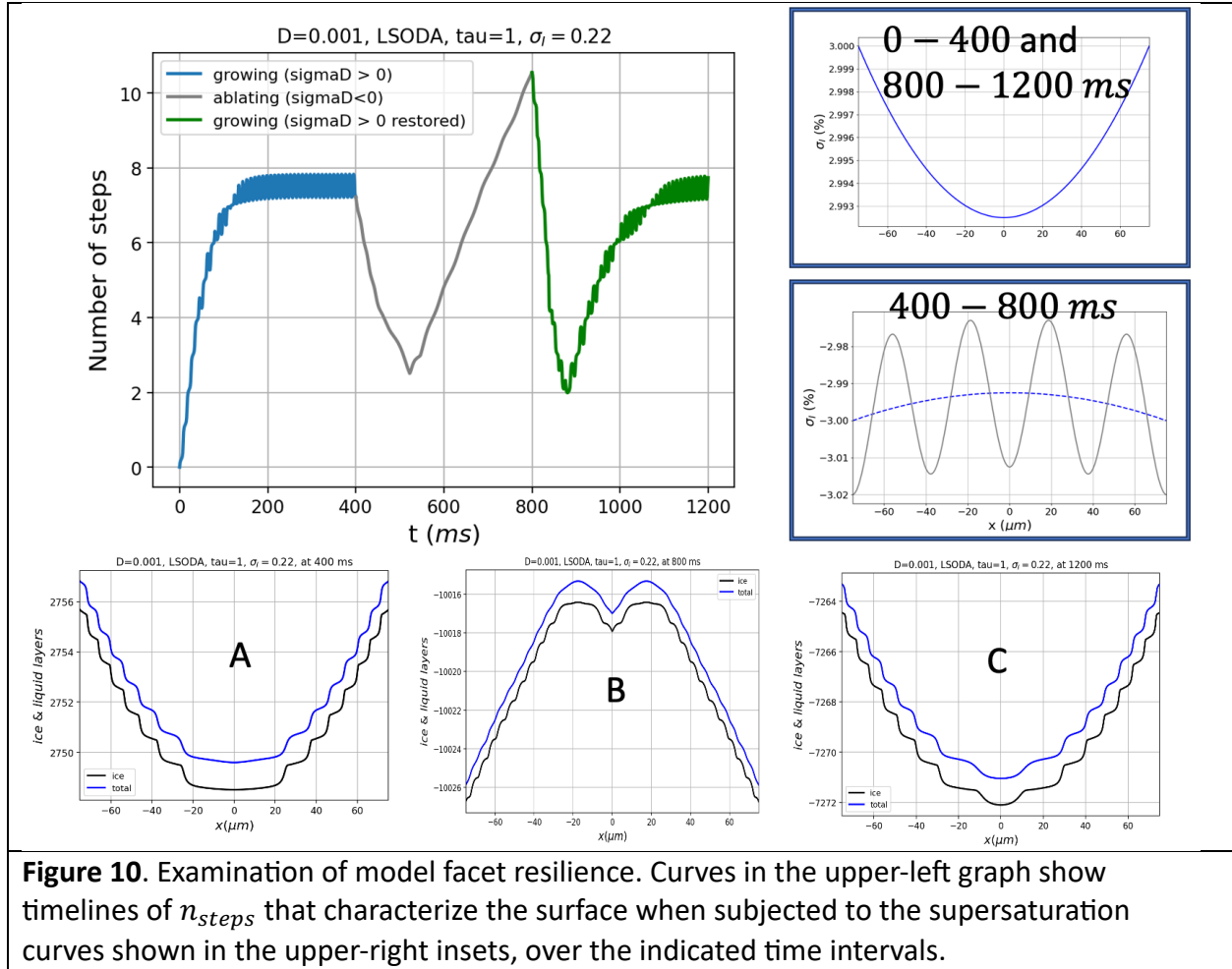
In ESEM experiments, facets exhibit a certain resilience, in that an initially faceted surface, after it is roughened by some perturbation, can usually be restored to its initial smooth faceted state after the initial conditions are restored. An example is shown in Fig. 9, in which the fraction of smooth, faceted area is seen to increase as a result of lowered temperature.

**Figure 9.** SEM images showing the fraction of smooth, faceted area increasing as a result of lowered temperature (top to bottom).



What resilience, if any, is exhibited by modeled facets? Figure 10 is an examination of this question.





The sequence of images in Fig. 10 begins with an initially-flat profile, which is then subjected to the following sequence:

1. From 0 to 400 *ms*, the surface is been exposed to the supersaturated water vapor curve shown in the inset located in the upper right part of the figure. By 400 *ms*, the profile has evolved to the faceted, steady-state profile labeled “A”.
2. From 400 to 800 *ms*, a perturbation is introduced in the form of the subsaturated water vapor curve shown in the inset located in the middle-right part of the figure. During this time, the surface evolves into the highly perturbed state labeled “B”.
3. From 800 to 1200 *ms*, the initial supersaturated water vapor regime is restored. During this time, the surface recovers its pre-perturbation faceted profile labeled “C”.

Conclusion ... qualitatively, QLC-2 exhibits resilience analogous to that of real crystal facets, such as the one shown in Fig. 9. We should hasten to add, however, the perturbed states exhibit vastly different vertical scales. That is, in Fig. 10, the perturbed profile seen at 800 *ms*, caused by the perturbation begun at 400 *ms*, is non-faceted (i.e., “rough”) only on the order of a few dozen monolayers of ice, whereas the actual crystal shown in Fig. 9 exhibits ridge-to-valley depths on the order of thousands of monolayers.

## 7. Summary and discussion

The QLC-2 model presented here offers significant technical improvements over the QLC-1 model reported in N2016, in that its numerical solutions are more stable, and its parameterizations are better constrained by independent numerical simulations of the overlying vapor field, i.e., the dependence of the center reduction parameter ( $c_r$ ) on crystal size ( $L$ ).

More fundamentally, QLC-2's equations of motion embody a more faithful atomistic representation of ice/QLL freeze/melt equilibration. That connection, in turn, enables the theory to represent a more unified picture of ice surface dynamics than has previously been possible. The model predicts, for example, facet convexity and concavity under growth and ablation conditions (respectively), a pattern that is echoed in reconstructions of SEM-grown ice crystals. The model also provides a mechanism by which real ice crystals resist dendritic geometries when subjected to supersaturation conditions (i.e., faceted growth), and how they also resist rounding when subjected to subsaturation conditions (faceted ablation). It is, essentially, a theory of faceting that rests fundamentally on atomistic variations in the thickness and volatility of the quasi-liquid layer that are exposed as a crystal grows or ablates.

The model also predicts a certain resilience to perturbations – also echoed by real ice crystals – in that faceted surfaces that have been disrupted in some way recover when conditions favorable to faceting are restored.

QLC-2 makes an unexpected qualitative prediction about characteristic distances, quantified here as  $\bar{\lambda}$ , the mean distance between adjacent layers of ice. We find that  $\bar{\lambda}$  separates mathematically as a product of two functions: one is a linear function of dimensionless variable,  $z \equiv \left( \frac{D}{L v_{kin}} \right)^{1/2}$ , and the other is a highly nonlinear function of the surface supersaturation. We find that the latter is an asymmetrical function of the surface supersaturation, such that growth conditions lead to smaller values of  $\bar{\lambda}$ , while ablation conditions lead to larger values of  $\bar{\lambda}$ , for comparable departures from equilibrium. We have no ready explanation for this behavior, but we do note that SEM observations are consistent with these observations in the sense that ridges in rough facets of growing crystals are spaced more closely than in rough facets of ablating crystals. As noted previously, this coincidence is subject to a very big caveat, namely, that the depths of these characteristic distances are vastly different in QLC-2 compared to experiment: in the former it is a few monolayers, while in the latter it is thousands of monolayers.

Our results have qualitative implications regarding morphological changes of cirrus cloud particles. As such particles fall through Earth's atmosphere, such crystals will encounter increased pressure, hence smaller  $D_{vap}$ , but also increased temperatures (unless there is an atmospheric inversion), hence larger  $D_{vap}$ . When the effect of increased pressure dominates, QLC-2 predicts enhanced growth at facet corners, hence greater facet convexity, and therefore a greater propensity toward hollowed crystal structures. When the effect of increased temperature dominates, however, we can expect more regular hexagonal shapes. Although

there is no single observational datum that would help us resolve these predictions, we can comment that in exceptionally cold regions (such as the Antarctic Plateau), or even in mid-latitudes where high-altitude cryo-capture of ice crystals on ground-launched balloons is possible, observations have shown that cirrus clouds are frequently hollowed, suggesting dominance of increased pressure.

We can also expect that because different facet types (basal, prismatic, or pyramidal) have distinct underlying crystal cell structures, their quasi-liquid properties will also be distinctive. Exploratory numerical studies varying the thickness of a single “layer” of ice has shown that a proportional increase in  $\bar{\lambda}$  results. Preliminary numerical experiments varying  $N^*$  and  $\bar{N}$  have shown that ...

A separate speculation concerns the observation that the  $D^{1/2}$  dependence of  $\bar{\lambda}$  values exhibited by QLC-2 is the same as in Turing patterns. In one sense this should come as no surprise, since Turing’s theory, like QLC-2, is based on a reaction-diffusion equation. But there are also very big differences, including the fact that Turing’s analysis proceeds from an analysis of sensitivity to perturbations to an initially homogeneous distribution of chemical species, whereas the patterns in QLC-2 emerge as steady states of the equations of motion.

Finally, we note that the atoms-to-mesoscale approach represented in QLC-2 is not as fully integrated as we would like it to be. In particular, if the temperature and pressure dependence in the vapor field calculations could be integrated with QLC-2, we would be able to take into account feedbacks that are not present within QLC-2 alone. The problem is the difference in time scales: vapor equilibration takes place hundreds of times faster than QLC-2 surface calculations. [But maybe Jake’s heterogeneous multiscale approach is the way forward on that].

## Appendix 1 – ESEM/GNBF retrieval

Here is a summary of key equations and constraints in the ESEM/GNBF retrieval ...

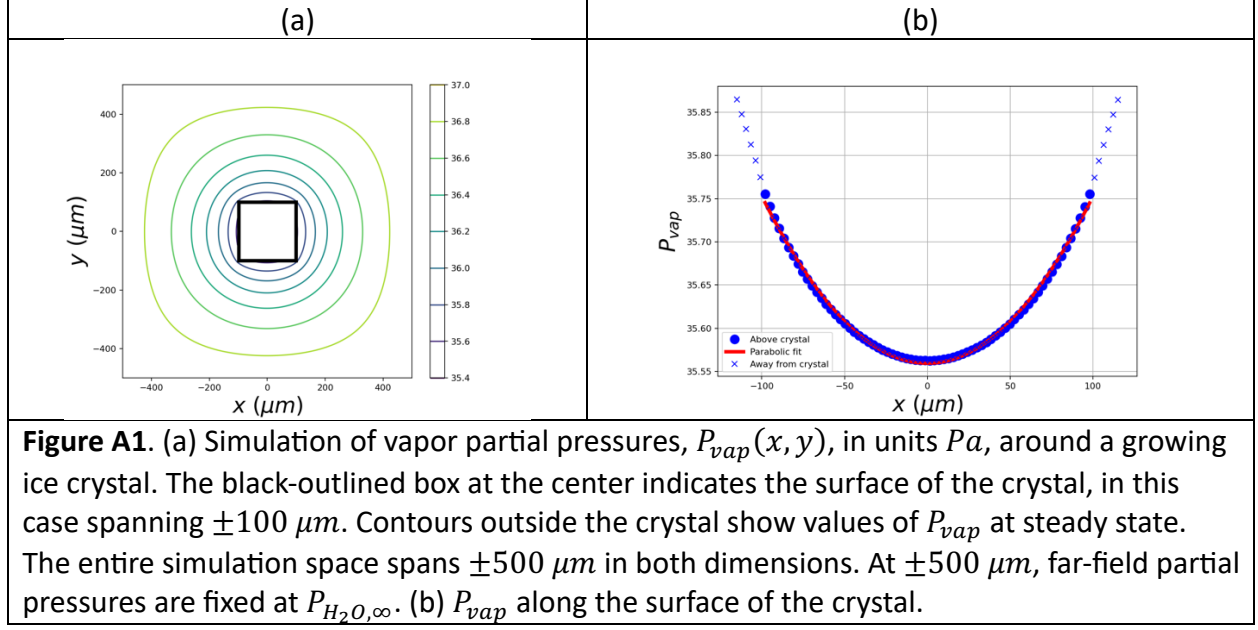
## Appendix 2 – Vapor field code

Simulation of the water vapor partial pressure,  $P_{vap}(x, y)$ , in the space surrounding a square-shaped crystal shown in Fig. A1(a), was achieved by integrating the two-dimensional diffusion equation

$$\frac{\partial P_{vap}}{\partial t} = D_{vap} \nabla^2 P_{vap} + - g_{ice} \times \rho_{ice} \times \frac{RT}{M_{H_2O} \Delta y} \quad (A1)$$

where  $D_{vap}$  is the diffusion coefficient of water vapor through air, which is computed by (based on a fit to data given in the Engineering Toolbox),

$$D_{vap} = D_{vap}^o \left( \frac{P_{amb}}{1 \text{ atm}} \right)^{-1} \left( \frac{T_{amb}}{273 \text{ K}} \right)^{m_D} \quad (A2)$$



The last term on the right of Eq. A1 implements Neumann boundary conditions that represent depletion of water vapor in the layer adjacent to the crystal surface due to crystal growth. Variables appearing in this term are:

- $g_{ice}$  is the specified growth rate of the ice surface; it equals zero except at the surface of the ice crystal, where its value is prescribed as  $g_{ice,s}$  (typically  $2 \frac{\mu m}{s}$ ).
- $\rho_{ice}$  is the mass density of ice,  $1.1 \frac{g}{cm^3}$ ;
- $M_{H_2O}$  is the molar mass of water,  $18 \frac{g}{mol}$ ; and
- $\Delta y$  is the spatial discretization in the  $y$ -direction (typically,  $\Delta x = \Delta y = 2.8 \mu m$ ).

Dirichlet conditions, representing the far-field vapor concentration ( $P_{vap, \infty}$ ), are imposed at the outside boundary of the simulation space.

Integration over time was performed using Euler's method, i.e., with time steps  $dt$ , and distance intervals  $\Delta x$  (which equals  $\Delta y$ ). That is, at each time step, changes in  $P_{vap}(x, y)$  were computed by

$$dP_{vap} = D_{vap} \nabla^2 P_{vap} dt - g_{ice} \times \rho_{ice} \times \frac{RT}{M_{H_2O} \Delta y} dt \quad (A3)$$

Parameters for the integration are given in Table A1. The resulting vapor concentration contours shown in Fig. A1(a) are seen to decrease with proximity to the crystal, as expected since the growing crystal is drawing water vapor out of the surrounding air. This reduction is greater at facet center compared to facet corners, in a roughly parabolic fashion, as shown in the profile in

Fig. A1(b), thus justifying the form  $\sigma_I(x) = \sigma_{I,corner} \times \left( c_r \left( \frac{x}{L} \right)^2 + (1 - c_r) \right)$  given in Eq. 6 of the text, where the “center reduction” is defined by

$$c_r(\%) \equiv \frac{P_{vap,surf}(corner) - P_{vap,surf}(center)}{P_{vap,surf}(corner)} \times 100 \quad (A4)$$

For example, in A1(b),  $c_r \approx 0.4\%$ .

| <b>Table A1. Parameters for simulation of the vapor field around a growing, square-shaped ice crystal</b> |  |
|---|--|
| Simulation space dimensions   | $X = Y = \pm 500 \mu m$                      |
| Time step for integration   | $dt = 5 \times 10^{-5} \mu s$                |
| Time interval for integration   | $t_{max} = 2 \mu s$                          |
| Spatial discretization  | $dx = dy = 2.8 \mu m$                        |
| Diffusion coefficient at $T_{amb} = 273 K$ , $P_{amb} = 1 atm$  | $D_{vap}^o = 21.9 \mu m^2 / \mu s$           |
| Ambient temperature   | $T_{amb} = 240 K$                            |
| Ambient pressure  | $P_{amb} = 68.6 Pa$                          |
| Diffusion Temperature-correction exponent   | $m_D = 1.86$                                 |
| Diffusion coefficient under ambient conditions  | $D_{vap} = 3.49 \times 10^4 \mu m^2 / \mu s$ |
| Far-field water vapor partial pressure  | $P_{vap,\infty} = 29.6 Pa$                   |
| Far-field water vapor supersaturation   | $\sigma_I = 0.25$                            |
| Mass density of ice   | $d_{ice} = 0.9 g/cm^2$                       |
| Growth rate of ice surface  | $g_{ice,s} = 2 \mu m/s$                      |
| Slope parameter for $c_r(L)$ under ambient conditions:  | $c_r^o = 0.0057 \mu m^{-1}$                  |

Other simulation results (not shown) exhibit the expected property that higher far-field vapor concentrations,  $P_{vap,\infty}$ , lead to higher  $P_{vap,surf}$ . The consequence of this should be that crystals would grow faster under such conditions, and therefore offset some of the increased  $P_{vap,surf}$ , but that (negative) feedback is not built into Eq. A1, because  $g_{ice,s}$  is a fixed parameter.

Figure A2 shows simulation results as a function of the crystal edge length. Fig. A2(a) shows that the steady-state concentration of water vapor at crystal corners declines with increasing crystal size. This is expected, since a larger growing crystal means there is more crystal surface area drawing water vapor out of the air.

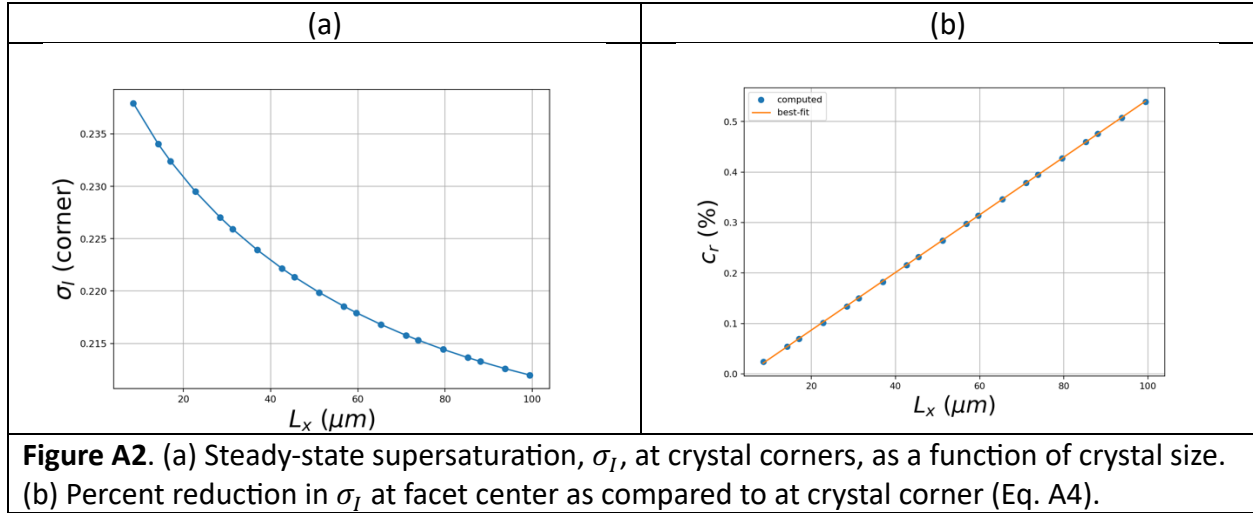


Fig. A2(b) shows the percent reduction in surface vapor concentration at facet center relative to facet corner (see the definition of  $c_r$  in Eq. A4).  $c_r(L)$  is seen to be a smoothly increasing function of crystal size, well-described by

$$c_r(L) = c_r^0 L \quad (\text{A5})$$

Other simulations (not shown) show that higher far-field vapor concentrations ( $P_{vap,\infty}$ ) do not greatly alter this parameterization. Also, this parameterization is entirely insensitive to  $\sigma_0$ . Because of this invariance,  $c_r(L)$  is more useful than  $P_{vap,surf}$  for describing the concentration of water vapor over a growing ice crystal facet.

Yet other simulations show that this parameterization is greatly affected by temperature (which reduces  $c_r^0$  considerably), and by the ambient pressure (which increases  $c_r^0$  considerably). Lower ambient temperatures and higher ambient pressures are both associated with smaller vapor diffusion coefficients,  $D_{vap}$ . Smaller  $D_{vap}$ , in turn, manifests as a more steeply curved  $P_{vap,surf}$  profile across the crystal surface, compared to the example shown in Fig. A1(b): it is harder for water vapor to diffuse across the facet surface when  $D_{vap}$  is small. The expected consequence is that lower ambient temperatures and higher ambient pressures will increase the tendency for excess growth at facet corners, ultimately leading to highly convex, indented, hollowed crystal morphologies, and even, at sufficiently small  $D_{vap}$ , dendritic forms such as snowflakes.

### Appendix 3 – Numerical considerations

Python, accelerated with Numby. Code and data are available on Github.

#### References:

The temperature dependence of the diffusion coefficient was based on data from [https://www.engineeringtoolbox.com/air-diffusion-coefficient-gas-mixture-temperature-d\\_2010.html](https://www.engineeringtoolbox.com/air-diffusion-coefficient-gas-mixture-temperature-d_2010.html)

## Other notes ...



Luis G. MacDowell

Mar 9, 2020

sent you the full-text you requested

*Dear Steven, thanks for your interest. Note Eq.8 of this paper, with a cosine term that resembles your ideas on Nesyba et al 2016. We found a way to work out the dynamics employed in Eq.8 and that yields a set of coupled equation...*

### Structure and fluctuations of the premelted liquid film of ice at the triple point

Preprint Mar 2020

Jorge Benet · Pablo Llombart · Eduardo Sanz · Luis G. MacDowell

Download full-text

Recommend preprint

Say thanks